

MULTIDIRECTIONAL SOLIDIFICATION MODEL FOR THE DESCRIPTION OF MICROPORE FORMATION IN SPRAY DEPOSITION PROCESSES

J.-P. Delplanque, E. J. Lavernia, and R. H. Rangel

*Department of Mechanical and Aerospace Engineering,
Department of Chemical and Biochemical Engineering and Materials Science,
University of California—Irvine, Irvine, California 92717, USA*

This article describes a numerical investigation of micropore formation in solidifying molten metal droplets impinging on a colder substrate. The velocity field inside the spreading liquid droplet is computed as a solution of the incompressible Navier-Stokes equations, and a volume-of-fluid function is defined in order to track the location of the free surface. A multidirectional solidification model is implemented to simulate the formation of possible pores, cavities, and/or troughs. This tracking algorithm allows for complex interface morphology representation as well as interface merging simulation. In the test case considered (high-velocity impact of a single droplet), simulations predict the formation of an annular trough on the surface of the solidified splat. This feature may be a precursor of pore or cavity formation in multiple-droplet cases.

INTRODUCTION

Spray deposition processes are an efficient means of manufacturing materials while saving energy and reducing costs, as they require significantly fewer manufacturing steps than conventional processes. Furthermore, the resulting materials have properties associated with rapid solidification such as fine-grained microstructures and nonequilibrium phases [1].

The fundamental problems associated with such processes are complex, since they involve high-velocity convective heat transfer with phase change and possibly breakup of the liquid phase. Accordingly, a growing number of investigations [2–9], both theoretical and experimental, concentrate on the fluid dynamics and/or heat transfer aspects of these processes. In the particular case of spray deposition, phenomena currently under investigation include quality of the splat/substrate contact [4, 6]; influence of substrate roughness on the quality of deposited materials [9]; influence of contact line dynamics on the spreading characteristics [7]; and droplet/splat, droplet/droplet, and droplet/particle interactions [3, 5], with or without solidification.

Received 20 October 1995; accepted 29 January 1996.

This work was sponsored in part by Sulzer Metco Inc. (Irvine, CA) and by NSF (CTS 92-24850). This research was also supported in part by the University of California, Irvine, through an allocation of computer resources.

Address correspondence to Dr. R. H. Rangel, Department of Mechanical and Aerospace Engineering, University of California—Irvine, Irvine, CA 92717-3975, USA.

Numerical Heat Transfer, Part A, 30:1–18, 1996

Copyright © 1996 Taylor & Francis

1040-7782/96 \$12.00 + .00

NOMENCLATURE

F	volume-of-fluid function	y	axial coordinate
\mathbf{F}_g	body forces	α	thermal diffusivity
\mathbf{g}	gravity acceleration	θ	volume fraction open to flow
h_{sf}	latent heat of solidification	λ	solidification constant
k	thermal conductivity	ρ	density
p	pressure	τ_R	reattachment time
s	curvilinear coordinate		
S	thickness of solidified layer		
Ste	Stefan number [$= k \Delta T / (\alpha \rho h_{sf})$]		
t	time		
T	temperature		
\mathbf{V}	velocity vector		
x	radial coordinate		

Subscripts

i	initial
l	liquid
m	at the melting point
s	solid

A major concern regarding spray deposition processes is the porosity of the resulting materials. Porosity affects the mechanical, electrical, and thermal performance of materials; it is present in spray-deposited materials, regardless of the experimental conditions selected or the materials being synthesized [2, 10, 11]. Depending on the application considered, porosity may be detrimental (applications requiring high strength and high resistance to cyclic deformation) or beneficial (e.g., in damping, thermal insulation, or self-lubrication applications). In any case, the successful commercial application of spray deposition as a viable manufacturing technology is critically dependent on our ability to understand the fundamental mechanisms that govern porosity formation.

Experimental investigations of porosity in spray-deposited preforms as a function of thickness [2] lead to the identification of three distinct regions: an upper band with a relatively high porosity percentage (surface porosity), a central portion with lower porosity percentage (steady state porosity), and a lower band with a porosity percentage (substrate porosity) comparable to that of the upper band. Candidate mechanisms leading to porosity formation include [2] gas entrapment [12], incomplete filling of the interstices between solid and/or partially solidified droplets [10, 13], and solidification shrinkage [2].

The formation mechanisms and quantitative calculation of microporosity during droplet impingement and solidification have been addressed only recently [2, 4, 5, 9]. The results obtained so far pertain mostly to substrate porosity. Simulations of a fully liquid droplet impinging on a solid substrate show that good contact between the splat and the substrate is generally obtained, whereas liquid ejection is produced if the droplet strikes on another splat [5]. A fully liquid ring colliding with a flattening splat causes the liquid to bounce, and may result in the formation of voids [5]. The numerical study of deforming molten-metal droplets as they interact with other droplets and/or a nonflat substrate provides further insight concerning the fundamental mechanisms governing pore formation in spray-processed materials [9]. If the roughness width is larger than the initial droplet diameter, the liquid undergoes a succession of accelerations and decelerations and, eventually, breaks up. If the droplet is larger than the roughness width,

the spreading process is hindered. Recent simulations reveal that the spreading liquid may separate from the solidifying splat [4], thus indicating that the commonly used solidification models and algorithms cannot adequately describe the rest of the process, since they assume a preferred direction of growth.

The research effort described herein focuses on the numerical investigation of micropore formation in spreading and solidifying molten-metal droplets as they impinge on a colder substrate. The primary objective of this work is to develop a multidirectional solidification algorithm adapted to the identification of possible micropore formation mechanisms in order to isolate the primary controlling factors and subsequently determine ways to reduce porosity in spray-processed materials.

FLUID DYNAMICS

The approach chosen is numerical. The fluid dynamics is simulated, while the solidification process is modeled. The velocity field inside the spreading liquid droplet is computed as a solution of the incompressible Navier-Stokes equations, and a volume-of-fluid function is defined in order to track the location of the free surface using a computer program called RIPPLE.

This code, developed at Los Alamos National Laboratory, is suited for modeling transient, two-dimensional, incompressible fluid flow with surface tension on free surfaces of general topology [14]. The fluid flow equations,

$$\nabla \cdot (\theta \mathbf{V}) = 0 \quad (1)$$

$$\theta \frac{\partial \mathbf{V}}{\partial t} + \nabla \cdot (\theta \mathbf{V} \mathbf{V}) = -\frac{\theta}{\rho} \nabla p + \frac{\theta}{\rho} \nabla \cdot \boldsymbol{\tau} + \theta \mathbf{g} + \theta \mathbf{F}_b \quad (2)$$

are solved using a two-step projection method. Here, θ is a function that characterizes the presence of internal obstacles ($\theta = 1$ in the fluid or void and 0 in obstacles). A cell in which $0 < \theta < 1$ is only partially open to the flow (θ is then an average over the cell). An underlying assumption in Eq. (1) is that $\partial\theta/\partial t$ is negligible. The validity of this assumption lessens as the characteristic time for solidification becomes comparable to the droplet spreading time. The particular case considered here is that of a high-impact velocity. Therefore this assumption is deemed valid. Low-impact-velocity cases would require modifications to RIPPLE's algorithm in order to include the effects of the θ time dependence. The advection term is evaluated using a second-order upwind, weakly monotonic scheme (Van Leer) [14]. The Poisson equation for the pressure field yielded by the second step is solved with an incomplete Choleski conjugate gradient method chosen for its speed and robustness [14]. The position of the free surface is obtained by solution of a volume-of-fluid transport equation:

$$\frac{\partial}{\partial t}(\theta F) + \nabla \cdot (\theta F \mathbf{V}) = 0 \quad (3)$$

where F is the volume-of-fluid function ($F = 1$ in the fluid and 0 in the void). A cell in which $0 < F < 1$ is only partially filled with fluid (F is then an average over

the cell). Surface tension effects are described using the continuum surface force (CSF) approach [15]. The details of the numerical analysis can be found in the work by Kothe et al. [14].

Since computations start at the time of impact, the computational domain must extend axially to include the complete incident drop. Furthermore, the resulting splat radial size is typically 1 order of magnitude larger than the initial droplet radius. Another constraint arises from the need for higher accuracy in the evaluation of surface tension forces, which diverge exponentially at breakup, thus drastically limiting the magnitude of the maximum time step. Note that a proper computation of breakup is pivotal in the determination of porosity.

UNIDIRECTIONAL SOLIDIFICATION

The unidirectional solidification model has been extensively described elsewhere [4, 5, 9] and is therefore only outlined here. This model is based on two main assumptions. First, it is assumed that the solidification proceeds as a moving front such that the phases are separated by the isotherm corresponding to the melting temperature. Second, the existence of a principal direction of heat flow within most of the physical domain leads to a unidimensional approximation of the actual heat transfer. Under these hypotheses, the splat solidification problem reduces to the one-dimensional motion of the solid-liquid interface. The interface can only move orthogonally to and away from the substrate. It is further assumed that the interface motion can be approximated by Neumann's solution to the Stefan problem (semi-infinite domain) [16].

This solution yields the thickness of the solidification layer as

$$S = 2\lambda\sqrt{\alpha_s(t - t_i)} \quad (4)$$

where t_i is the time at which solidification started. The solidification constant λ is obtained from the heat balance at the interface:

$$\lambda = \frac{1}{\sqrt{\pi}} \left(\frac{\text{Ste}_s}{\text{erf}(\lambda) \exp(\lambda^2)} - \frac{\text{Ste}_l \sqrt{\alpha_l/\alpha_s}}{\text{erf}(\lambda \sqrt{\alpha_s/\alpha_l}) \exp(\lambda^2 \alpha_s/\alpha_l)} \right) \quad (5)$$

where Ste_s and Ste_l are the solid and liquid Stefan numbers,

$$\text{Ste}_s = \frac{k_s(T_m - T_s)}{\alpha_s \rho_s h_{sf}} \quad \text{Ste}_l = \frac{k_l(T_l - T_m)}{\alpha_l \rho_l h_{sf}}$$

The solidifying layer is then treated as an internal obstacle to the flow of the spreading liquid metal. The corresponding values of θ are deduced from the local values of S . Rangel and Bian [17, 18] have discussed the effect of liquid motion and provided results that account for liquid motion in the calculation of the solidification rate.

Spray Deposition Simulations

A case representative of spray deposition conditions is considered (reference case). A 30- μm tungsten droplet at 3750 K (melting temperature is 3650 K) impinges on a flat substrate maintained at 1500 K with an impact velocity of 400 m/s. This large value of the velocity was chosen because it is the higher bound of the parametric range of interest for spray deposition processes and it constitutes a severe test of the numerical algorithm limitations.

The predicted behavior is presented in Figure 1. The deforming solid line represents the 0.9 contour line of F (the volume-of-fluid fraction). At impact, the liquid in contact with the substrate starts to solidify, thus forming a solid layer—the primary solidification disk (PSD). In a very short time (less than 0.045 μs), the PSD height is large enough for the very high velocity (more than twice the impact velocity) liquid metal flowing on top of it to detach in a manner akin to that observed in liquid-jet flow over a backward facing step. The liquid jet reattaches to the substrate at $t = \tau_R$ (about 0.065 μs), leaving a gap (a possible pore) between the solidified layer's edge and the reattachment point. Solidification also starts at the reattachment point to form a solid ring—the secondary solidification ring (SSR).

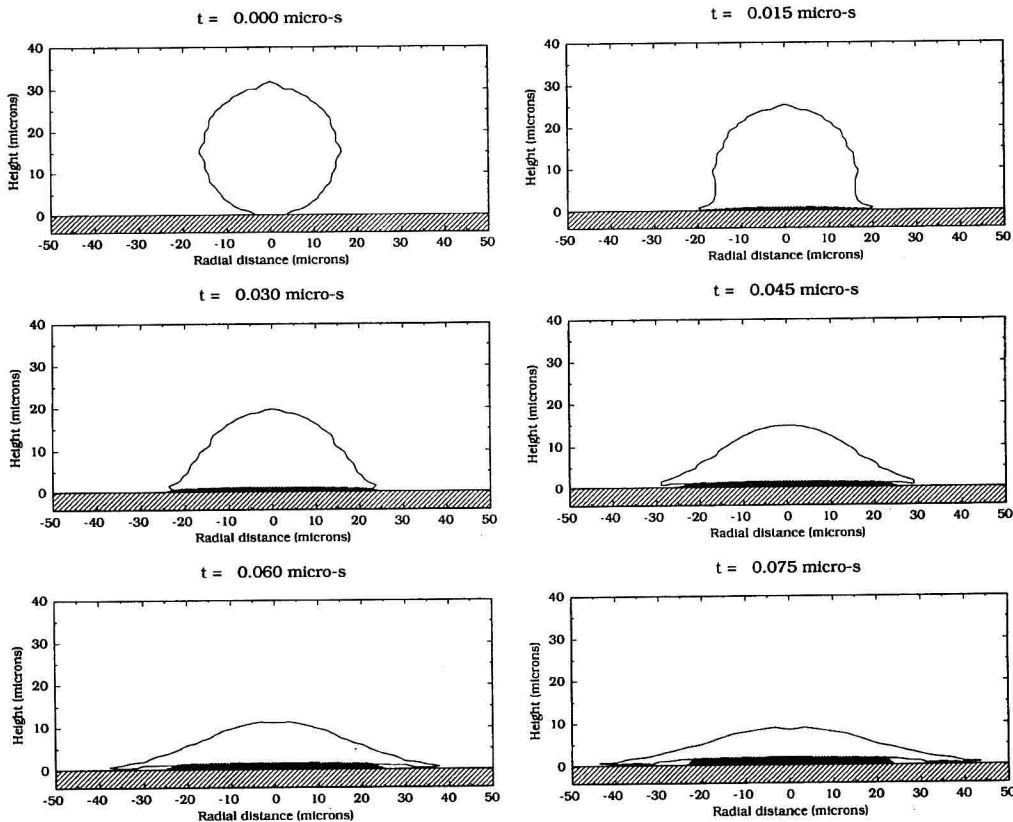


Figure 1. Tungsten droplet solidification sequence. Unidirectional solidification model.

If the computations are continued beyond this point with the unidirectional solidification model, the spreading and solidification processes proceed until all liquid has been solidified ($\approx 0.225 \mu\text{s}$). The final state is a central solid disk surrounded by a void ring followed by a solid ring. Owing to growth subsequent to reattachment, the gap is smaller than it was initially (at τ_R), but it is not completely filled. Results beyond τ_R are not shown because the solidification model is obviously inadequate. Multidirectional solidification must be allowed, so that possible solidification of the liquid bridge connecting the PSD and the SSR may occur.

A micropore formation mechanism is consequently proposed (cf. Figure 2):

1. Impact of the droplet on the substrate with instantaneous onset of unidirectional solidification.
2. Formation of the PSD: deformation of the droplet with radial liquid flow acceleration and simultaneous unidirectional solidification.

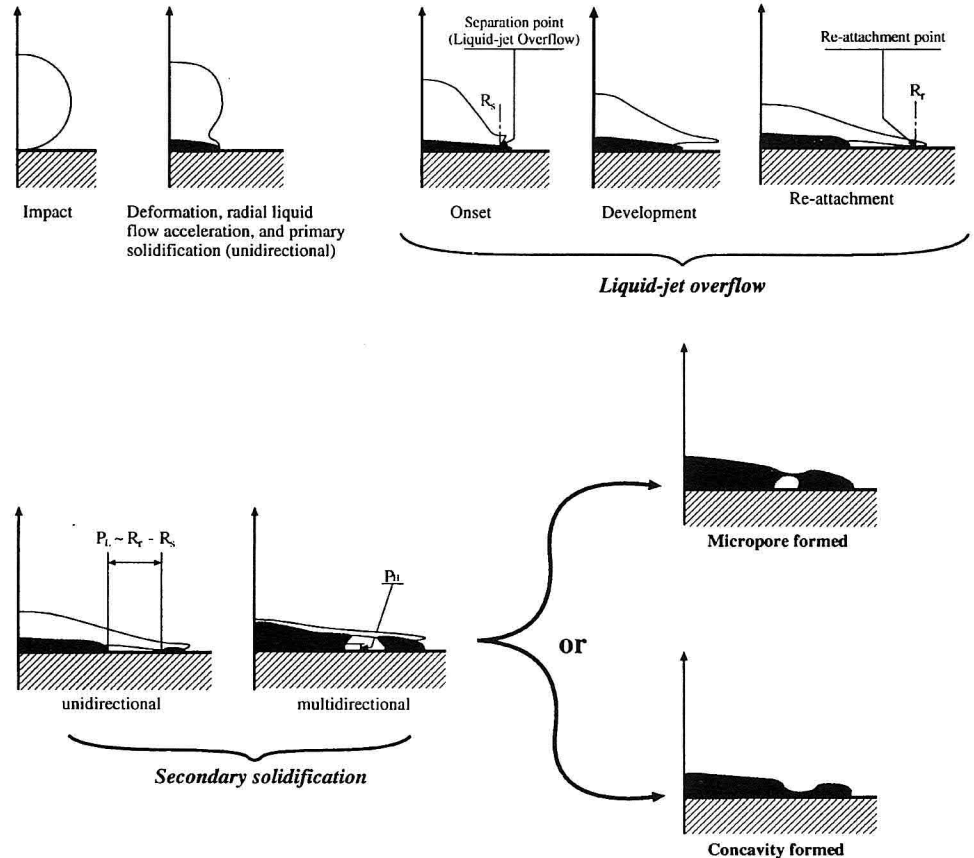


Figure 2. Proposed micropore formation mechanism.

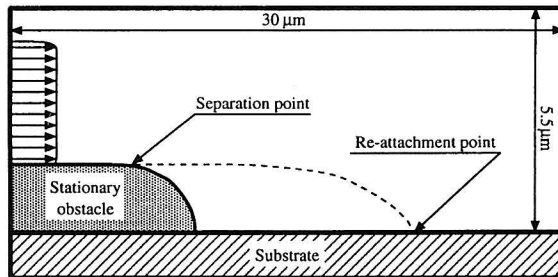


Figure 3. Case setup of liquid-jet overflow (aspect ratio not preserved).

3. Liquid-jet overflow: onset and development of a liquid layer extending radially without touching the substrate.
4. Reattachment of the liquid layer to the substrate ($t = \tau_R$), and onset of unidirectional solidification at the reattachment point (formation of the SSR).
5. Secondary solidification (phase I): simultaneous growth of PSD and SSR.
6. Secondary solidification (phase II): possible transversal solidification of the liquid layer connecting PSD and SSR (multidirectional solidification).

If the liquid bridge completely solidifies, a micropore is formed. Partial or no solidification of the liquid bridge could result in the formation of a circular trough (concavity) on the solidified-splat surface or leave the splat surface unaffected if the gap between PSD and SSR is completely filled. A multidirectional solidification model is necessary to describe micropore formation by this mechanism.

Liquid-Jet Overflow

It is noteworthy that good mesh resolution is critical to the prediction of this phenomenon. In fact, if the mesh used is too coarse (of the order of $1 \mu\text{m}$ at the substrate in the above-mentioned case), the simulations fail to predict liquid-jet overflow. It is necessary to decrease the mesh size to $1/3 \mu\text{m}$ close to the substrate to correctly predict the overflow.

A test case (cf. Figure 3) was designed to further investigate liquid-jet overflow. This configuration is meant to schematize the flow behavior in the liquid-jet overflow region, near the edge of the PSD. Liquid tungsten is injected parallel to the top of a stationary disk (radial wall-jet). The dimensions of the disk (diameter $10 \mu\text{m}$, height $2 \mu\text{m}$) are consistent with the size of the PSD observed in the reference case reported above.

The characteristics of the jet (thickness $2 \mu\text{m}$, initial velocity 800 m/s) are also consistent with those of the liquid tungsten layer near the edge of the solidifying splat. By limiting the computational domain, this simplified configuration allows a much finer mesh ($0.2 \times 0.2 \mu\text{m}$) than is possible in the droplet impact case. Figure 4 shows the predicted evolution of the free surface from initial injection to reattachment. The action of surface tension reduces the initial jet

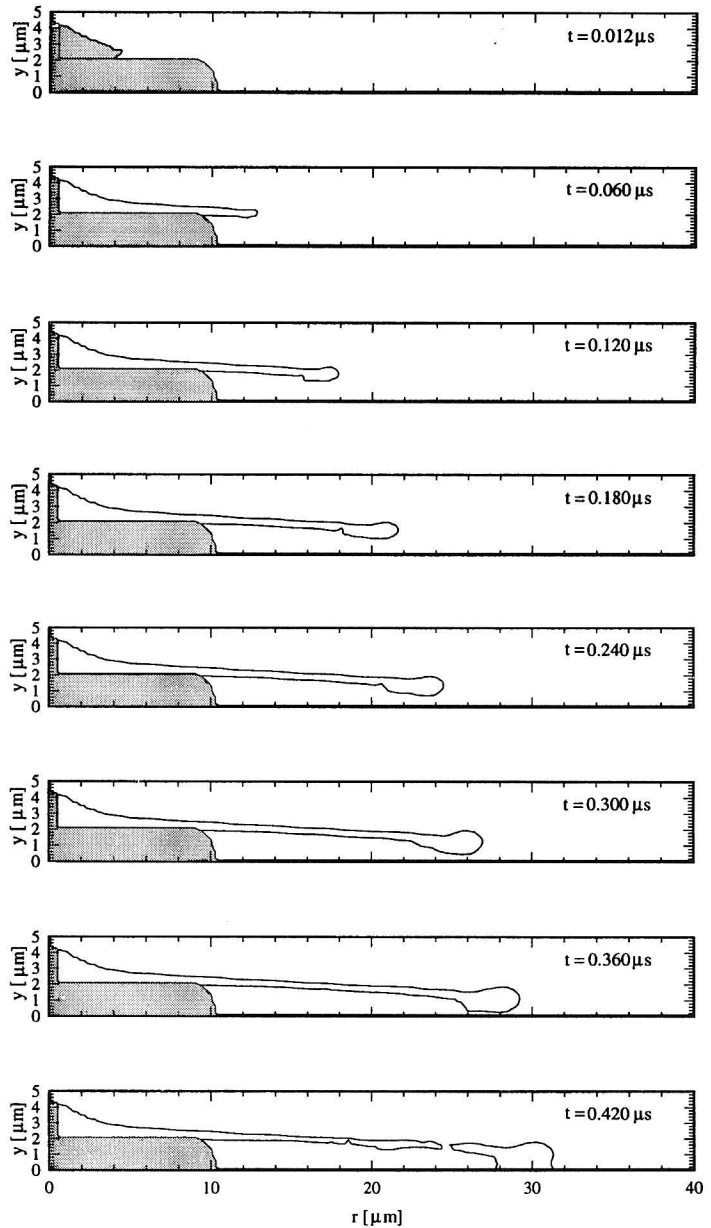


Figure 4. Liquid-jet overflow.

thickness to about $1 \mu\text{m}$ near the splat edge. This phenomenon also induces a downward velocity, which causes the liquid to reattach much sooner than it would under the action of gravity only. The edge of the liquid layer assumes a rounded shape as a result of the action of surface tension forces. It reattaches at about $0.4 \mu\text{s}$. Breakup occurs just after reattachment. In droplet impact cases, the stagnation

flow pattern also contributes to the downward velocity, thus reducing the distance between the PSD edge and the reattachment point and inhibiting breakup. This simulation shows that the mesh used in the droplet-impact calculations reported above gives a qualitatively satisfactory description of the liquid-jet overflow phenomenon.

MULTIDIRECTIONAL SOLIDIFICATION

The multidirectional solidification model is based on the application of a locally one-dimensional (1-D) energy balance in the direction normal to the solid-liquid interface. The unidirectional model allowed growth orthogonally to the substrate only. Note that the mechanism defined above will possibly yield more than one interface, and the possibility of interface merging also has to be considered. In fact, the possible solidification of the liquid bridge mentioned above would result from interfaces merging. The implementation of this model therefore requires the definition of an efficient tracking algorithm for the solid-liquid interfaces.

Solid-Liquid Interface Tracking

The solid-fluid interfaces are tracked using uniformly distributed markers. The tracking algorithm developed here is based upon a tracking method previously used to simulate the dynamics of vortex lines [19]. This algorithm allows for complex interface morphology representation as well as interface merging simulation.

Each interface $\{is\}$ is fitted with N markers uniformly spaced along it and numbered 1 to N (index i). The position of each marker in the physical space (x_i, y_i) is related to the curvilinear coordinate s_i :

$$ds_i = \sqrt{dx_i^2 + dy_i^2} \quad (6)$$

The markers move continuously as the solid layer grows and are not necessarily located on mesh lines. The first step is to determine the logical coordinates (I, J) of the cell in which a marker (i) is located. These indices also give access to both components of the corresponding normal (n_{xi}, n_{yi}) . Let $P_i(x_i, y_i)$ be the location of a marker at an interface at time t and let l_i be the length of growth at $P_i(x_i, y_i)$ during the time interval dt (the evaluation of l_i is discussed below). Then the location of the marker at time $t + dt$, $M_i(X_i, Y_i)$, is given by

$$(X_i, Y_i) = (x_i + l_i n_{xi}, y_i + l_i n_{yi}) \quad (7)$$

It is possible that l_i is such that (X_i, Y_i) is beyond the liquid-void interface (overshoot) because, as will be seen below, the growth rate evaluation essentially assumes an unlimited liquid. In this case, (X_i, Y_i) is taken at the intersection of the liquid-void interface and the direction of growth.

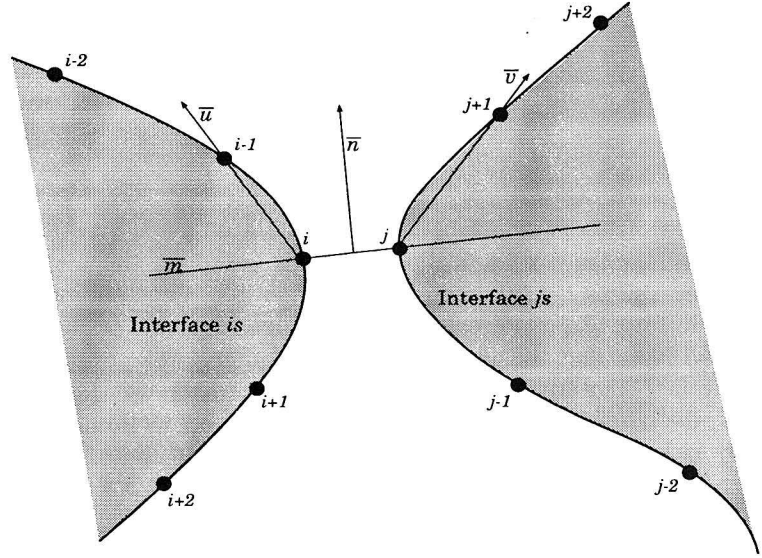


Figure 5. Merging of two interfaces.

The curvilinear s_i coordinate of M_i on the new interface is related to s_{i-1} :

$$s_i = s_{i-1} + \sqrt{(X_i - X_{i-1})^2 + (Y_i - Y_{i-1})^2} \quad (8)$$

with the convention that $s_1 = 0$. At this point, the smallest rectangle enclosing each interface $\{is\}$ is computed.

Interfaces are defined as “active” if they are growing. This requires that they be, at least partially, in contact with some liquid. Merging occurs when the distance between two markers (i and j) on two active interfaces ($\{is\}$ and $\{js\}$) is less than a given criterion (typically of the order of the mesh spacing). Both interfaces are then split into two branches at their respective merging points M_i and M_j . To determine which pairs of branches should be reconnected, vectors $\mathbf{u} = \overline{M_i M_{i-1}}$ and $\mathbf{v} = \overline{M_j M_{j-1}}$ are compared (see Figure 5). If $\mathbf{u} \cdot \mathbf{v} > 0$, branch $[1, i]$ of $\{is\}$ is connected with branch $[1, j]$ of $\{js\}$; otherwise, it is connected with branch $[j, N_j]$ of $\{js\}$. The resulting interfaces are then renumbered, and the markers on each interface are uniformly redistributed to maintain accuracy. This algorithm can also treat cases of self-merging where two portions of the same interface merge.

From the fluid dynamics point of view, the growing solid splat is an internal obstacle to the fluid flow. The solid interface data provided by the marker locations must therefore be related to the volume fraction open to flow (θ , see Eqs. (1) and (2)). To this end, an algorithm, akin to Youngs’ piecewise linear interface calculation [20] algorithm, was written that yields the fractional area defined in a given cell by a geometrical point and a direction.

Solid Growth

The growth rate is evaluated by writing the interface heat balance:

$$k_s \frac{\partial T_s}{\partial x} = k_l \frac{\partial T_l}{\partial x} + \rho h_{sf} \frac{\partial S}{\partial t} \quad (9)$$

If the liquid heat flux is neglected (near melting point conditions), the growth rate can then be approximated by

$$\frac{\partial S}{\partial t} \approx \frac{k_s}{\rho h_{sf}} \frac{T_m - T_s}{L} \quad (10)$$

where L is a characteristic thickness of the solid splat. On the other hand, if the 1-D Stefan solution, Eq. (4), is used, the growth rate expression is

$$\frac{\partial S}{\partial t} = \frac{2\lambda^2\alpha_s}{S} \quad (11)$$

where λ is given by Eq. (5).

The two approaches, Eq. (10) and Eq. (11), coincide only if the liquid heat flux is also neglected in the 1-D Stefan approach and for small values of Ste_s (cf. Eq. (5)). Furthermore, the characteristic length L must be chosen equal to S . The 1-D Stefan solution, Eq. (11), is therefore less constraining than the interface energy boundary condition. The numerical problem yielded by the singularity of this expression at the initial time ($S = 0$) is circumvented by using Eq. (4) instead during the first few time steps. This is legitimate in the case of droplet impact and solidification, since as shown above, the growth process is initially unidirectional.

In the original Stefan problem, S is the thickness of the solid layer. More generally, it represents the length of the heat flow path from the considered interface point to the substrate. In the case investigated here, this heat flow path may be substantially distorted by the presence of pores within the solidified layer (cf. Figure 6).

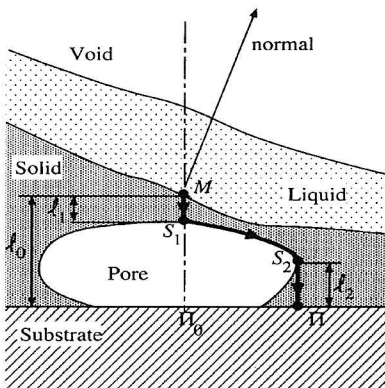


Figure 6. Estimation of the heat transfer path for solidification above a pore.

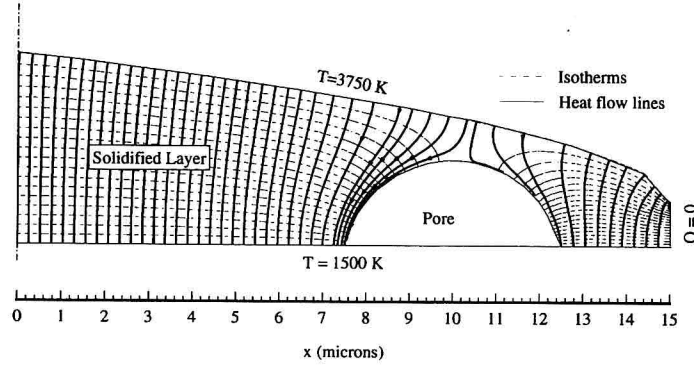


Figure 7. Finite element simulation of heat conduction in a solidified layer with a hemispherical pore.

A finite element analysis of a model heat-conduction problem in a 2-D parabolic tungsten splat with a hemispherical pore was performed to assess the extent of the distortion induced on the heat-flow lines. The top of the splat was maintained at a constant temperature (3750 K) and so was the substrate (1500 K). A no-heat-flux condition was enforced at the edge of the splat ($x = 15 \mu\text{m}$) because it is usually not in contact with the liquid. There is negligible conduction through the pore (Figure 7). The computations show that the induced distortion of the heat-flow lines is restricted to a small region around the pore. Therefore the length of the heat-flow line from a point M on the top of the splat and above a pore to the substrate may be approximated by the shortest distance from this point to the substrate $\mathcal{L} = l_1 + (s_2 - s_1) + l_2$, where s_1 and s_2 are the curvilinear coordinates of S_1 and S_2 along the pore boundary (Figure 6). Consequently, the growth rate is approximated as

$$\frac{\partial S}{\partial t} = \frac{2\lambda^2\alpha_s}{\mathcal{L}} \quad (12)$$

Boundary Conditions

For each time step, the fluid dynamics equations are solved first, followed by the volume-of-fluid transport equation, and finally, the solid-liquid interface is moved according to the solidification model described above. After each incremental solidification, the values of θ and F must be updated to reflect the new solid-liquid interface position. In cells that are completely included in the region between the previous position of the interface and the new one, θ is set to 1 and F to zero. In interfacial cells, the value of θ corresponding to the marker position and its normal is calculated using a locally linear approximation of the interface shape. If there is more than one marker in a given interfacial cell, an average

maker position and an average normal are used. In order to evaluate the new value of F , consider the case where the volume of liquid V_l , in a given cell (total volume \mathcal{V}) is only affected by solidification; there is no fluid inflow or outflow (this corresponds to the algorithm described above). Mass conservation requires that

$$\frac{V_s^o}{\mathcal{V}} + \frac{V_l^o}{\mathcal{V}} = \frac{V_s}{\mathcal{V}} + \frac{V_l}{\mathcal{V}} \quad (13)$$

where superscript o denotes the value before solidification. Since $F = V_l/(V_l + V_v)$ and $\theta = (V_l + V_v)/\mathcal{V}$ (where subscript v refers to the void), this can be recast to yield the new value of the volume-of-fluid fraction after solidification:

$$F = 1 + \frac{\theta^o}{\theta} (F^o - 1) \quad (14)$$

This equation also gives the maximum value that the solid fraction $\gamma (= 1 - \theta)$ can reach given an initial fluid volume (F^o):

$$\gamma_{\max} = \frac{V_f^o + V_s^o}{\mathcal{V}} = 1 - \theta^o(1 - F^o) \quad (15)$$

This criterion is a limit to the growth imposed by the amount of liquid available.

Multidirectional Growth and Merging Test Case

The model developed above is first tested without fluid dynamics effects. Two test cases are considered.

The first case is designed to test the ability of the model to take into account heat-line distortions induced by the presence of a pore. The initial configuration is shown in Figure 8a. A 3- μm -wide and 1.5- μm -thick layer of liquid tungsten at

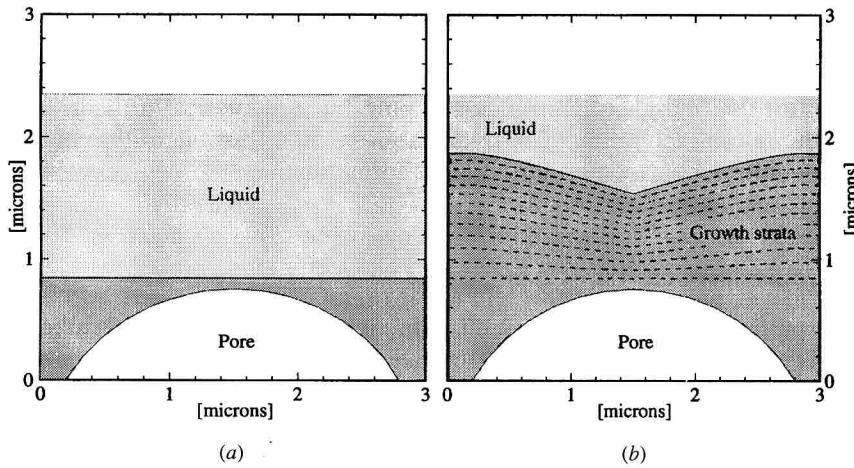


Figure 8. Solidification above a pore—test case: (a) initial configuration and (b) after 0.045 μs .

3750 K rests on top of a 0.85- μm layer of solidified tungsten in which there is a spherical-cap-shaped pore with a 2.6- μm base and a maximum height of 0.75 μm . The substrate, at $y = 0$, is maintained at 1500 K. Figure 8b shows the predicted shape after 0.045 μs as well as the computed intermediate growth strata (0.004 μs apart). As expected, the solidification process is significantly affected by the presence of the pore. In order to quantify this effect, a heat-line distortion parameter (χ) is defined as the ratio of the distorted heat-line length at a given point on the interface to the distance from that point to the substrate. For points on the interface that are not above the pore, $\chi = 1$. At any given time, the maximum value of χ is observed at the interface point just above the pore's apex (M). Initially, χ is about 2 at M and, moving along the interface, smoothly decreases to 1. This indicates that the growth at M is 2 times slower than that which would be observed if there were no pore. Then, as the interface moves away from the pore, the heat transfer is less affected because the height of the pore becomes a smaller portion of the total heat-line length. For the last stratum computed here, $\chi_{\text{max}} \approx 1.5$. Note that the slope of the interface at M becomes discontinuous (i.e., the radius of curvature of the interface at this point is smaller than the mesh resolution) because growth occurs along the normal to the interface (Figure 8b). This analysis confirms that when a pore is formed, it significantly hinders heat transfer in the solid layer above it. This causes the solidification process to slow down in this region and leads to the formation of a trough. This feature is propitious to the subsequent formation of another pore.

The purpose of the second test case is to verify the ability of the model to simulate the merging of growing interfaces. A 2-D pool ($3 \times 0.7 \mu\text{m}$) of liquid tungsten at 3750 K is considered (Figure 9a). At $t = 0$, two sinusoidally shaped solids at 1500 K are plunged from above into the pool. Solidification ensues (Figure 9b), first on both peaks independently, then with successive merging of the interfaces. Here again, growth strata are separated by 0.004 μs . Computations were stopped when the outer interface reached the domain boundary. The mesh ($0.1 \times 0.07 \mu\text{m}$) was not overly refined, in order to remain consistent with the constraints inherent to larger scale computations of practical cases. Consequently, the computed final shape (Figure 9c) is not smooth. The irregularities show the limitations of the mesh resolution. Similarly, the void appearing in the middle of the pool (on the merging plane) is not a pore but a numerical artifact; its size is below the mesh resolution. These tests show that this algorithm adequately represents interface dynamics during pore formation.

Droplet Impact Test Case

A preliminary test of the application of the multidirectional solidification algorithm to spray deposition was performed. The conditions are identical to those of the reference case reported above and previously treated with the unidirectional solidification model. The predicted initial behavior, from impact to reattachment (0.08 μs), is essentially unchanged, since as expected, the solidification is unidirectional in this phase (cf. Figure 10). After $t = 0.08 \mu\text{s}$, the splat thickness is large

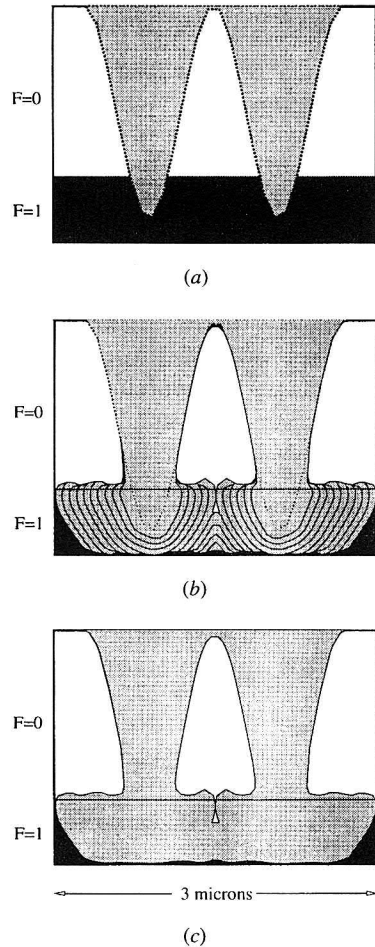


Figure 9. Multidimensional growth and merging test case: (a) initial shape, (b) solidification strata, and (c) final shape.

enough for curvature effects to influence significantly the growth process; multidirectional solidification starts.

Just after reattachment, the SSR undergoes unidirectional solidification, with the liquid spreading on the horizontal solidified layer. When the SSR is thick enough for multidirectional solidification to affect the growth process ($0.150 \mu s$), the high velocities in the liquid layer (of the order of 100 m/s radially) cause some liquid to impinge the growing inner edge of the SSR. Hence, in addition to the expected outward radial spreading of the SSR, multidirectional solidification causes the SSR to grow and spread inward, thus reducing the gap formed by liquid-jet overflow. Therefore, in the case considered here, transversal solidification of the liquid bridge between the PSD and the SSR is not predicted. Instead, the computed final splat shape ($0.300 \mu s$) shows an annular trough on the splat top

(Figure 11). This feature is reasonably resolved (six cells deep, four cells wide), given the relative coarseness of the mesh used for this test case. The depth of the depression (about one-third of the maximum splat height) seems large enough to promote liquid breakup and thus to enhance micropore formation in the case of multiple-droplet impacts, as previous studies on the influence of surface roughness on droplet spreading have shown [9]. The solidification algorithm developed here has an inherent bias resulting from the conversion of the Lagrangian tracking of the solid front to the Eulerian representation of the volume open to flow by means of function θ . For the test case considered herein, this bias yields a mass conservation discrepancy typically of the order of 15%. Note that the accuracy is also affected by the astringently large magnitude of the droplet impact velocity. Furthermore, the qualitative trends obtained here are limited to the specific case considered and should not be generalized. Indeed, work is continuing to investigate thoroughly and quantitatively the effect of multidirectional solidification on spray deposition processes. In particular, lower impact velocity may allow freezing of the

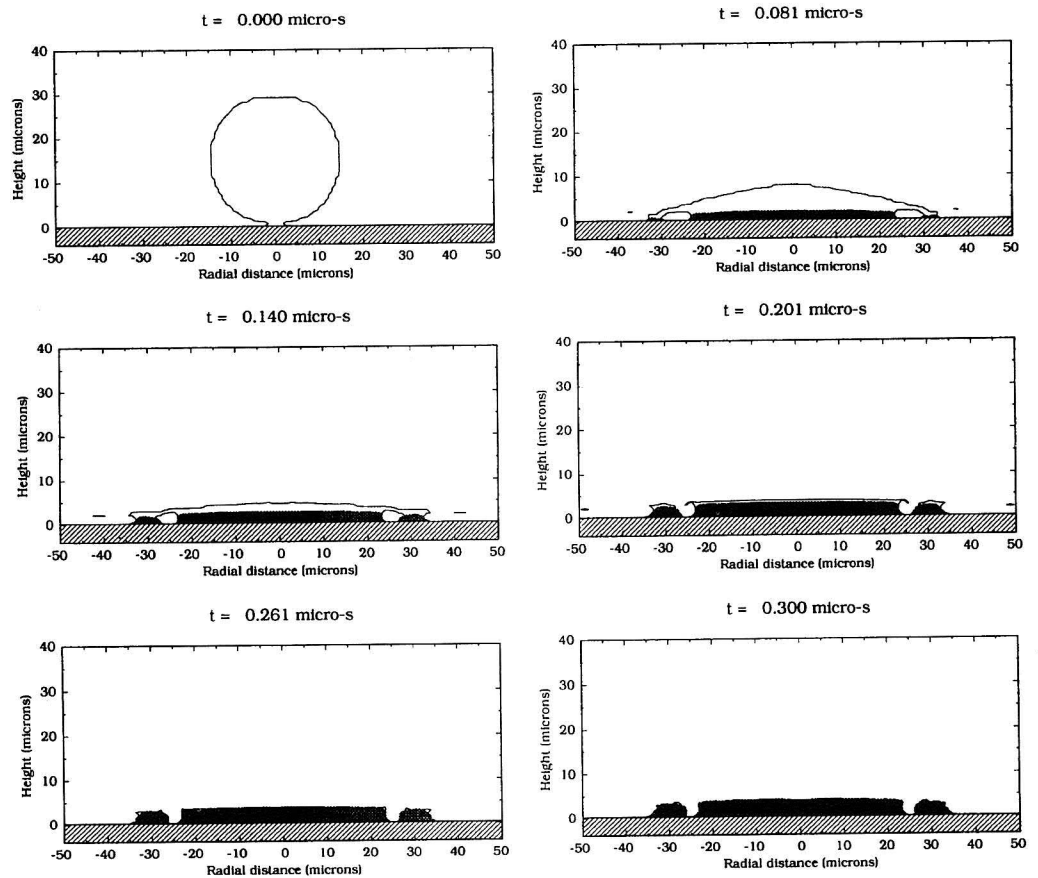


Figure 10. Tungsten droplet solidification sequence. Multidirectional solidification model.

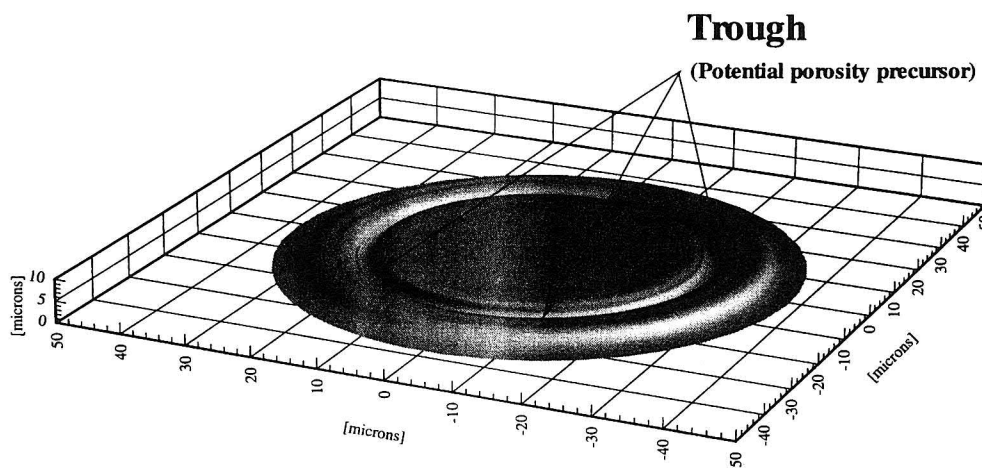


Figure 11. Tungsten droplet solidification. Predicted final splat morphology.

liquid bridge between the PSD and the SSR, thus forming a micropore underneath. However, low-impact-velocity cases would require modifications of the fluid dynamics model, as the quasi-steady solidification assumption is no longer valid in those cases.

CONCLUSIONS

A multidirectional solidification model was defined to simulate the formation of possible pores and/or concavities in spray deposition processes. This model is based on the application of a locally 1-D solution where the solid front advances in the direction normal to the solid-liquid interface. The multiple solid/fluid interfaces are tracked using uniformly distributed markers. The tracking algorithm allows for complex interface morphology representation as well interface merging simulation.

In the test case considered (high-velocity impact of a single droplet), no direct pore formation was observed. However, simulations predict the formation of a circular trough on the surface of the solidified splat. This feature may be a precursor of pore formation in multiple-droplet cases.

REFERENCES

1. H. Liu, R. H. Rangel, and E. J. Lavernia, Modeling of Droplet-Gas Interactions in Spray Atomization of Ta-2.5W Alloy, *Mater. Sci. Eng. A*, vol. 191, pp. 171-184, 1995.
2. E. Lavernia and Y. Wu, *Spray Atomization and Deposition*, John Wiley, New York, 1995 (in press).
3. G. Trapaga, E. F. Matthys, J. J. Valencia, and J. Szekely, Fluid Flow, Heat Transfer, and Solidification of Molten Metal Droplets Impinging on Substrates—Comparison of Numerical and Experimental Results, *Metall. Trans. B Process Metall.*, vol. 23B, pp. 701-718, 1992.

4. H. Liu, E. J. Lavernia, and R. H. Rangel, Numerical Investigation of Micro-Pore Formation During Substrate Impact of Molten Droplets in Plasma Spray Processes, *Atomization Sprays*, vol. 4, pp. 369–384, 1994.
5. H. Liu, E. J. Lavernia, and R. H. Rangel, Numerical Simulation of Substrate Impact and Freezing of Droplets in Plasma Spray Processes, *J. Phys. D: Appl. Phys.*, vol. 26, pp. 1900–1908, 1993.
6. J. Fukai, Z. Zhao, D. Poulikakos, C. M. Megaridis, and O. Miyatake, Modeling of the Deformation of a Liquid Droplet Impinging on a Flat Surface, *Phys. Fluids*, vol. 5, no. 11, pp. 2588–2599, 1993.
7. D. M. Anderson and S. H. Davis, Local Fluid and Heat Flow near Contact Lines, *J. Fluid Mech.*, vol. 268, pp. 231–265, 1994.
8. P. Grant, B. Cantor, and L. Katgerman, Modelling of Droplet Dynamics and Thermal Histories During Spray Forming, III: Analysis of Spray Solid Fraction, *Acta Metall. Mater.*, vol. 43, no. 3, pp. 913–921, 1995.
9. H. Liu, E. J. Lavernia, and R. H. Rangel, Modeling of Molten Droplet Impingement on a Non-Flat Surface, *Acta Metall. Mater.*, vol. 43, no. 5, pp. 2053–2072, 1995.
10. S. Annavarapu, D. Apelian, and A. Lawley, Processing Effects in Spray Casting of a Steel Strip, *Metall. Trans. A Phys. Metall. Mater. Sci.*, vol. 19A, pp. 3077–3086, 1988.
11. J. Zhang, M. N. Gungor, and E. J. Lavernia, The Effect of Porosity on the Microstructural Damping Response of 6061 Aluminum Alloy, *J. Mater. Sci.*, vol. 28, no. 6, pp. 1515–1524, 1993.
12. D. B. Morris and M. Morris, Rapid Solidification of Ni_3Al by Osprey Deposition, *J. Mater. Res.*, vol. 6, no. 2, pp. 361–365, 1991.
13. E. J. Lavernia, The Evolution of Microstructure During Spray Atomization and Deposition, *Int. J. Rapid Solidification*, vol. 5, no. 1, pp. 47–85, 1989.
14. D. B. Kothe, R. C. Mjolsness, and M. D. Torrey, RIPPLE: A Computer Program for Incompressible Flows with Free Surfaces, Technical Rept. LA-12007-MS, UC-000, Los Alamos National Laboratory, Los Alamos, N. Mex., 1991.
15. J. U. Brackbill, D. B. Kothe, and C. Zemach, A Continuum Method for Modeling Surface Tension, *J. Comput. Phys.*, vol. 100, pp. 335–354, 1992.
16. H. S. Carslaw and J. C. Jaeger, *Conduction of Heat in Solids*, 2nd ed., Oxford University Press, New York, 1959.
17. R. H. Rangel and X. Bian, The Inviscid Stagnation-Flow Solidification Problem, *Int. J. Heat Mass Transfer*, vol. 39, no. 8, pp. 1591–1602, 1996.
18. R. H. Rangel and X. Bian, Numerical Solution of the Inviscid Stagnation-Flow Solidification Problem, *Numer. Heat Transfer Part A Applications*, vol. 28, pp. 589–603, 1995.
19. R. H. Rangel and W. A. Sirignano, Nonlinear Growth of Kelvin-Helmoltz Instability: Effect of Surface Tension and Density Ratio, *Phys. Fluids*, vol. 31, no. 7, pp. 1845–1855, 1988.
20. W. Rider and D. Kothe, Stretching and Tearing Interface Tracking Methods, Paper AIAA-95-1717, presented at the 12th AIAA CFD Conference, San Diego, Calif., 1995.